Journal of Alloys and Compounds 900 (2022) 163516

Contents lists available at ScienceDirect

Journal of Alloys and Compounds

journal homepage: www.elsevier.com/locate/jalcom

Research Article

Preparation and characterization of nonstoichiometric Te-deficient and Te-rich thermoelectric $Bi_{2-x}Gd_xTe_{3\pm y}$ compounds

Maxim Yaprintsev[a], Alexei Vasil'ev[b], Oleg Ivanov[a,b,*]

[a] Belgorod State University, Belgorod 394015, Russian Federation
[b] Belgorod State Technological University named after V.G. Shukhov, Belgorod 308012, Russian Federation

ARTICLE INFO

Article history:
Received 28 October 2021
Received in revised form 23 December 2021
Accepted 27 December 2021
Available online 30 December 2021

Keywords:
Bismuth telluride
Electronegativity
Rare earth elements doping
Spark plasma sintering
Nonstoichiometric compounds
Thermoelectric properties

ABSTRACT

The Gd-doped Bi_2Te_3 compounds were prepared by solvothermal synthesis and spark plasma sintering. It was found that for the $Bi_{2-x}Gd_xTe_{3\pm y}$ compounds with x = 0.01; 0.05; 0.1; 0.15 and 0.2, the Gd doping results in relevant changing the Te content, y, i.e. x and y are inter-dependent. Governing by the Gd content, the Te-deficient $Bi_{2-x}Gd_xTe_{3-y}$ compositions with x = 0; 0.01; 0.05 and y = 0.018; 0.011; 0.003, and the Te-rich $Bi_{2-x}Gd_xTe_{3+y}$ compositions with x = 0.1; 0.15; 0.2 and y = 0.013; 0.023; 0.04, were successfully prepared. The Te-vacancies and the anti-site Bi_{Te} defects are specific for the Te-deficient compositions, whereas the interstitial Te atoms and the anti-site Te_{Bi} defects are characteristic for the Te-rich compositions. Deviation from Te-stoichiometry is originated from high-temperature Te evaporation under sintering. The Te-enriched starting $Bi_{2-x}Gd_xTe_3$ powders were applied to tune the Te-stoichiometry in desired manner. A rate of the Te evaporation decreases with increasing x that is related to difference in electronegativites of the Bi and Gd atoms, which, in turn, results in increasing the strength of polar covalent Gd-Te bond as compared to that for polar covalent Bi-Te bond. Crystal lattice parameters, concentration and mobility of electrons, thermoelectric properties, and grain ordering degree are different for the nonstoichiometric Te-deficient and Te-rich compositions. Highest thermoelectric figure-of-merit is found for the Te-deficient $Bi_{1.99}Gd_{0.01}Te_{2.989}$ composition (ZT≈0.7 at ~400 K).

1. Introduction

Energy conversion efficiency between heat and electricity in thermoelectric material is characterized by its thermoelectric figure-of-merit, $ZT=TS^2/\rho k$, where T is absolute temperature, S is Seebeck coefficient, ρ is specific electrical resistivity and k is total thermal conductivity with contributions from crystal lattice and carriers [1]. Lower thermal conductivity and specific electrical resistivity, and higher Seebeck coefficient should be at the same time combined in thermoelectric material to maximize its ZT value. The challenge lies in the fact that these thermoelectric properties are intimately but adversely inter-dependent. As result, optimizing one property often degrades other properties. To decouple these thermoelectric properties, usually it is necessary in thermoelectric material to form defects of various nature [2–10]. At present, bismuth telluride, Bi_2Te_3, and Bi_2Te_3-based alloys with n- and p-types of conductivity are the best materials for low-temperature thermoelectric applications [11–13]. Unfortunately, the thermoelectric efficiency of these materials also remains to be too low until now (ZT≈1). To improve the thermoelectric properties of Bi_2Te_3 and Bi_2Te_3-based alloys, a number of investigations using various physical and technological approaches have been carried out [14–24]. The core of these investigations is based on defect engineering. Some of key defects remarkably affecting the thermoelectric properties of Bi_2Te_3-based alloys are naturally formed during a high-temperature treatment of these alloys, which is accompanied by destroying their stoichiometry. Actually, it is known that energy of Te evaporation (52.55 kJ mol^{-1}) is much lower than that of Bi (104.80 kJ mol^{-1}) [25]. Hence, at high temperatures Te is evaporated much easier than Bi. Decreasing the Te content results in forming the Te vacancies in crystal Bi_2Te_3 structure. These Te-deficient Bi_2Te_{3-x} compounds are nonstoichiometric compounds of cation vacancy type. It should be noted that forming Te vacancies can result in forming relevant anti-site defects of Bi in Te-sites (Bi_{Te}) [26,27]. There are also ways to prepare nonstoichiometric Te-rich Bi_2Te_{3+x} compounds of cation interstitialcy type, in which destroying Te-stoichiometry usually results in forming interstitial Te atoms and anti-site defects of Te in Bi-sites (Te_{Bi}) as structure elements of the material [28,29]. Via

* Corresponding author at: Belgorod State University, Belgorod 394015, Russian Federation.
E-mail address: Ivanov.Oleg@bsu.edu.ru (O. Ivanov).

https://doi.org/10.1016/j.jallcom.2021.163516
0925-8388/

various mechanisms, both the Te vacancies and the anti-site Bi_{Te} defects in Bi_2Te_{3-x} compounds, and the interstitial Te atoms and the anti-site Te_{Bi} defects in Bi_2Te_{3+x} compounds can be believed to will affect the thermoelectric properties of the nonstoichiometric Te-deficient and Te-rich Bi_2Te_3-based compounds.

The purpose of this paper is to prepare the nonstoichiometric Te-deficient and Te-rich $Bi_{2-x}Gd_xTe_{3\pm y}$ compounds and characterize features in their elemental composition, crystal structure, microstructure and thermoelectric properties. To tune a desired deviation from Te-stoichiometry, firstly, Te-enriched starting $Bi_{2-x}Gd_xTe_3$ powders were applied to prepare relevant bulk samples by spark plasma sintering (SPS), and, secondly, Gd doping of the bulk samples resulting in a partial substitution of Gd for Bi was also involved. Detailed mechanisms of this tuning in Te-stoichiometry will be discussed below.

2. Materials and methods

To prepare the starting $Bi_{2-x}Gd_xTe_3$ powders with x = 0.01; 0.05; 0.1; 0.15 and 0.2, solvothermal synthesis was applied. Analytically pure chemicals ($Bi(NO_3)_3{\cdot}5H_2O$, TeO_2, $Gd(CH_3COO)_3{\cdot}4H_2O$, NaOH, poly(1-ethenylpyrrolidin-2-one), ethane-1,2-diol) were used for this synthesis. $Bi(NO_3)_3{\cdot}5H_2O$ and $Gd(CH_3COO)_3{\cdot}4H_2O$ were taken in stoichiometric ratio in accordance with x, whereas TeO_2 was taken in excess on the basis that the excess tellurium content would be 3 at% in all the synthesized powders with different x. Hence, all the starting $Bi_{2-x}Gd_xTe_3$ powders were Te-enriched. The main stages of solvothermal synthesis were stages as follows: (*a*) $Bi(NO_3)_3{\cdot}5H_2O$, TeO_2 and $Gd(CH_3COO)_3{\cdot}4H_2O$ were dissolving in mixture of 450 cm^3 ethane-1,2-diol NaOH and 15 g NaOH under vigorous stirring by a magnetic stirrer; (*b*) poly(1-ethenylpyrrolidin-2-one) (M_r=12000) was added to the reaction mixture and this mixture was again under vigorous stirring for 30 min; (*c*) autoclave was sealed and maintained at 190 °C for 5 min and then cooled to room temperature naturally; (*d*) after completing the reaction, dark grey precipitate was taken out by centrifuging and washed with deionized water and ethyl alcohol several times and then dried at 80 °C for 8 h. To prepare the bulk samples, the starting powders were spark-plasma-sintered at pressure of 40 MPa and temperature of 680 K for 2 min in vacuum, resulting in the Ø20 mm× 15 mm cylinders. To examine the thermoelectric properties of the bulk $Bi_{2-x}Gd_xTe_3$ samples, 2 × 2 × 10 mm bars and Ø10 × 2 mm disks were prepared.

To identify crystal structure and phase composition of the starting powders and the bulk samples, X-ray diffraction (XRD) analysis was performed by using a Rigaku Ultima IV diffractometer with CuK_α-radiation. Scanning transmission electron microscopy (STEM) was used to characterize morphology of the starting powders (a JEM-2100 transmission electron microscope). To measure density of the bulk samples, the Archimedes method was involved. To determine correct elemental composition of the bulk samples, a Shimadzu ICP (Inductively Coupled Plasma) emission spectrometer ICPE-9000 was applied. To study grain structure features of the bulk samples, a scanning electron microscope (SEM) Nova NanoSEM 450 was used. The specific electrical resistivity and the Seebeck coefficient of the bar samples were measured by using a ZEM-3 system, whereas the total thermal conductivity of the disk-shaped samples was measured by a TC-1200 system using a laser flash method. A Mini Cryogen Free Measurements System (Cryogenic Ltd, UK) was also used to study the Hall effect and estimate concentration, n, and Hall mobility, μ_H, of majority carriers.

3. Results and discussion

According to XRD analysis, all the starting $Bi_{2-x}Gd_xTe_3$ powders with different x consist of major rhombohedral $R\bar{3}m$ phase that is typical for pure Bi_2Te_3, and minor trigonal $P321$ phase corresponding to elemental Te. Forming the minor Te phase could be expected, since excess Te content was specially introduced into all the starting powders. Difference between ionic radii of Bi^{3+} (1.020 nm) and Gd^{3+} (0.938 nm) is small enough [30]. As result, effect of the Gd doping on lattice Bi_2Te_3 parameters is too weak to be observed in XRD patterns, taken for compositions with different x. Therefore, the lattice parameters, a=b and c, for all the starting powders were x-independent and equal to 4.387 and 30.492 Å, respectively. According to STEM examination, all the starting $Bi_{2-x}Gd_xTe_3$ powders mainly consisted of hexagonal plate-shaped two-dimensional (2D) particles with average plate size of a few hundreds of nm and width of ~100 nm. STEM image of these particles in the powder with x = 0.1 is shown in inset to Fig. 1. Forming the plate-shaped 2D-particles during a chemical synthesis is typical for Bi_2Te_3-based compounds, which is originated from specific features in their crystal structure and chemical bonding [11–13,31,32]. Elemental composition of the $Bi_{1.9}Gd_{0.1}Te_3$ particles was earlier analyzed by the ICP emission spectrometer [33]. According to results of this analysis, Gd was in fact inserted in the particles, and all the elements (Bi, Gd, Te) were uniformly distributed within the particles.

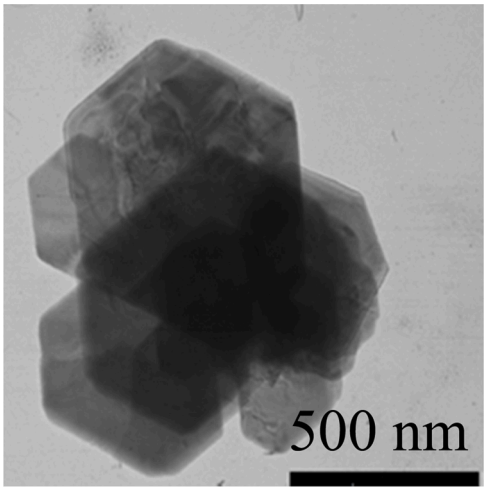

Fig. 1. STEM image of hexagonal plate-shaped 2D-particles in the starting $Bi_{1.9}Gd_{0.1}Te_3$ powder.

High-temperature sintering the starting $Bi_{2-x}Gd_xTe_3$ powders is unavoidably accompanied by Te evaporation, resulting in destroying Te-stoichiometry in relevant bulk samples. This Te evaporation was really observed in our experiments. Moreover, the Te content in the bulk $Bi_{2-x}Gd_xTe_3$ samples, SPS-prepared from the relevant starting powders with initial Te excess (3 at%) under the same conditions, happened to be x-dependent (Fig. 2(a)). With increasing x, the Te content is linearly increasing, too. Stoichiometry line corresponds to the composition with x = 0.06. The compositions with x < 0.06 are the nonstoichiometric Te-deficient compositions, whereas the compositions with x > 0.06 are the nonstoichiometric Te-rich compositions. Therefore, by changing the Gd content, Te-stoichiometry of the bulk $Bi_{2-x}Gd_xTe_3$ samples can be tuned between the nonstoichiometric Te-deficient and Te-rich compositions. Further these samples should be more correctly designated as $Bi_{2-x}Gd_xTe_{3\pm y}$ compositions with y = 0.018; 0.011; 0.003 (for the nonstoichiometric Te-deficient $Bi_{2-x}Gd_xTe_{3-y}$ compositions) and y = 0.013; 0.023; 0.04 (for the nonstoichiometric Te-rich $Bi_{2-x}Gd_xTe_{3+y}$ compositions) for x = 0.01; 0.05; 0.1; 0.15 and 0.2, respectively. The x and y coefficients are linearly connected to each other, i.e. x and y are inter-dependent. In general, increasing the Te content with increasing the Gd content can be originated from more strength of chemical Gd-Te bond as compared to that for Bi-Te bond. This strength will be mainly affecting an efficiency of the Te evaporation. In turn, the strength of a

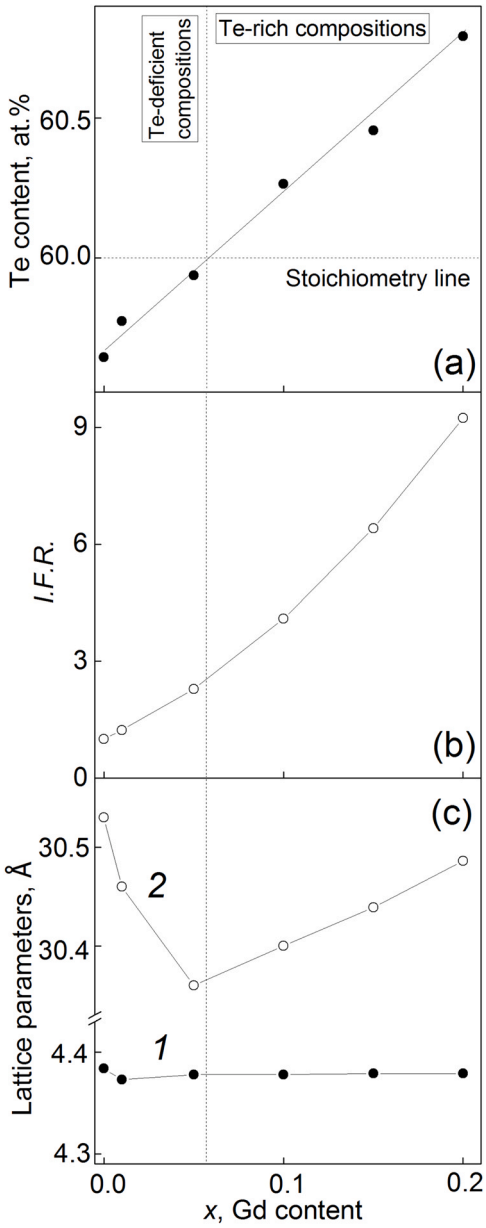

Fig. 2. The Gd content effect on: (a) the Te content, (b) the ionic fraction ratio, and (c) the lattice parameters *a* (curve *1*) and *c* (*2*) in the bulk $Bi_{2-x}Gd_xTe_{3\pm y}$ samples, SPS-prepared under the same conditions.

chemical bond depends on its energy, i.e. the greater energy results in the stronger strength. For the nonstoichiometric Te-deficient $Bi_{2-x}Gd_xTe_{3-y}$ compositions, the strength of Te bonding is weak enough, that results in strong the Te evaporation. In this case, even initial Te excess in the starting powders cannot compensate for its high-temperature evaporating, which results in forming the non-stoichiometric Te-deficient $Bi_{2-x}Gd_xTe_3$ composition. For the non-stoichiometric Te-rich $Bi_{2-x}Gd_xTe_{3+y}$ compositions, the strength of Te bonding is stronger, resulting in less strong the Te evaporation. In this case, initial Te excess in the starting powders can totally compensate for its high-temperature evaporating. Moreover, Te excess will also persist in the bulk $Bi_{2-x}Gd_xTe_{3+y}$ samples after SPS-treatment. Several processes can be involved in changing the strength of Bi(Gd)-Te bonds in the $Bi_{2-x}Gd_xTe_{3\pm y}$ compositions with changing the Gd content. First of all, difference in electronegativites of Bi and Gd should be taken into account. The crystal Bi_2Te_3 structure is known to be layered [11–13,31,32]. The five individual atomic layers are stacked in the following order.

Te(1)–Bi–Te(2)–Bi–Te(1), (1)

where Te(1) and Te(2) denote two types of Te in the Bi_2Te_3 lattice.

Crystal *c*-axis is oriented perpendicularly to the layers, whereas crystal (*a*–*b*)-planes are oriented along the layers. The Bi atoms are octahedrally coordinated by Te atoms, and the Te(2) atoms are octahedrally coordinated by the Bi atoms. The Te(1) atoms are covalently bonded with three Bi atoms on one side and by weaker Vander-Waals bonds with three other Te(1) atoms on the other side. The Bi-Te(1) bond length is close to the expected covalent bond length, while the Bi-Te(2) bond rather corresponds to the value that is expected for ionic bonding [31,32]. For Gd-doped Bi_2Te_3, an ionic bonding fraction, *I.F.*, which characterizes ionicity degree in a polar covalent bond, can be changed, since the electronegativity of the Bi and Gd atoms are remarkably different. In accordance with the empirical Pauling expression, *I.F.* is related to a difference between the electronegativities of interacting *A* (X_A) and *B* (X_B) atoms (ions) as follows [34].

$$I.F. = 1 - \left[exp\left\{ -\frac{(\Delta X)^2}{4} \right\} \right], \quad (2)$$

where $\Delta X = X_A - X_B$.

By a partial substituting *A* or/and *B* ions for other *C* ion (*C*-doping), *I.F.* can be increased (at $X_A - X_C > X_A - X_B$ or $X_C - X_B > X_A - X_B$ that will results in increasing ΔX) or decreased (at $X_A - X_C < X_A - X_B$ or $X_C - X_B < X_A - X_B$ that will results in decreasing ΔX). For the $Bi_{2-x}Gd_xTe_{3\pm y}$ compounds, electronegativities of elements are $X_{Bi} = 2.02$, $X_{Te} = 2.10$ CE $X_{Gd} = 1.20$ [35]. Since $X_{Te} - X_{Gd} > X_{Te} - X_{Bi}$, *I.F.* should be gradually increasing with increasing the Gd content. To roughly estimate changing in *I.F.*, which is due to the Gd-doping, expression (2) was applied. Difference in the Te(1)-Bi and Te(2)-Bi bonds was neglected. Since only partial substitution of Gd for Bi occurred, the $X_{Bi-Gd} = [(1-x) \cdot X_{Bi} + x \cdot X_{Gd}]$ expression was introduced to take into account changing the X_{Bi} and X_{Gd} contributions into the total electronegativity of the Gd-doped compounds with different *x*. The calculated *I.F.* values are too small, although relative change of *I.F.*, which is originated from the Gd-doping, is remarkably enough. To show this change, *I.F.* was recalculated to an ionic fraction ratio, $I.F.R. = I.F.(x)/I.F.(x = 0)$. The *I.F.R.* vs. Gd content dependence is shown in Fig. 2(b). *I.F.R* is expectedly growing with increasing *x*, and the maximum *I.F.R.* value is equal to ~9.25. The strength and the energy of polar covalent bond in semiconductors can be, at least, partially, governed by energy of chemical bond. In particularly, energy gap, *Eg*, of many semiconductors with polar covalent bonds increases with increasing this energy in accordance with empirical Manka expression [36].

$$E_g = a(E_S - b), \quad (3)$$

where E_S is the single bond energy, and *a* and *b* are the constants.

Really, for 52 binar semiconductors, their energy gap was found to be progressively increasing with increasing E_S [37]. This tendency is a result of increasing the ionicity degree (*I.F.R.*) in chemical bonds of these compounds. In accordance with the Pauling's approach, the energy of polar covalent bond should be increasing with increasing the iconicity degree, which is dependent on difference between the electronegativites of atoms being chemically bonding [38]. For two atoms, *A* and *B*, with the electronegativites of X_A and X_B, the energy of its bond can be calculated by the Pauling's method

$$E(A-B) = [E(A-A) + E(B-B)]^{1/2} + 30(\Delta X_{AB})^2, \quad (4)$$

where *E*(*A*-*A*) and *E*(*B*-*B*) are energies of a normal covalent bond between the same atoms and $\Delta X_{AB} = X_A - X_B$.

In accordance with expression (4), the gradual Gd doping of Bi_2Te_3 will result in relevant increasing of the ionic bonding fraction (Fig. 2(b)) and, hence, in relevant increasing of the energy bond. In

turn, this increasing the energy bond will weaken the high-temperature Te evaporation. As result, depending on the Gd content, the nonstoichiometric Te-rich and Te-deficient $Bi_{2-x}Gd_xTe_{3\pm y}$ compounds can be prepared.

XRD patterns of all the bulk $Bi_{2-x}Gd_xTe_{3\pm y}$ samples correspond to single phase with the space symmetry $R\bar{3}m$ group. No traces of other phases were found. However, although the crystal symmetry of the samples does not change with varying *x*, the crystal lattice is slightly changed with varying *x*. To analyze the crystal lattice changes, the *a* and *c* parameters were calculated by the Rietveld refinement. The *a*(*x*) and *c*(*x*) dependences are presented in Fig. 2(c). The *a* parameter can be believed to be *x*-independent (curve *1*). With increasing *x*, the c parameter is firstly falling for the Te-deficient compositions, and then it is gradually increasing for the Te-rich compositions. That is a clear boundary between the Te-deficient and Te-rich compositions exists. To explain this *a*(*x*) and *c*(*x*) behavior, it would be helpful to account for changing the Te content in different $Bi_{2-x}Gd_xTe_{3\pm y}$ samples, which is in turn governing by changing the Gd content (Fig. 2(a)). Decreasing the Te content for the Te-deficient compositions is naturally resulting in forming the Te vacancies within the crystal structure [39]. But in accordance with this mechanism, forming the Te vacancies will lead to decreasing the lattice parameters that is in contradiction with experimental data. Therefore, other mechanisms besides forming the Te vacancies should be involved. Forming the anti-site defects of Bi in Te-sites (Bi_{Te}) due to the Te evaporation at high temperatures can be taken as one of suitable mechanisms [26,27]. Ionic radii, *R*, of Bi^{3+} and Te^{2+} in the Bi_2Te_3 structure are remarkably different, $R(Bi^{3+})$= 1.020 nm against $R(Te^{2+})$= 0.089 nm [30]. Since $R(Bi^{3+})$ is bigger as compared to $R(Te^{2+})$, forming the Bi_{Te} defects will result in increasing the lattice parameters with increasing the Te vacancy content. Actually, the *c* parameter is steady increasing with decreasing the Te content for the Te-deficient compositions (curve *2* in Fig. 2(c)). For the Te-rich compositions, forming the interstitial Te defects will result in gradual increasing the lattice parameters with increasing the Te content. It should be noted that the anti-site Te_{Bi} defects can be also formed in the Te-rich $Bi_{2-x}Gd_xTe_{3+y}$ compositions. However, these defects cannot result in increasing the lattice parameters. Therefore, the *c*(*x*) behavior observed for the nonstoichiometric bulk $Bi_{2-x}Gd_xTe_{3\pm y}$ samples can be attributed to forming the specific point defects. These defects are the anti-site Bi_{Te} defects for the Te-deficient compositions, and the interstitial Te atoms for the Te-rich compositions. Since $c >> a$, the *a*(*x*) features found in the *c*(*x*) behavior is expressed much weaker (curve *1* in Fig. 2(c)).

Density of all the bulk samples was found to be weakly and irregularly *x*-dependent. Maximum density value is equal to ~7.64 g·cm^{-3} for $x = 0.1$ that is ~99.2% of theoretical value of the Bi_2Te_3 density (7.7 g/cm^3), and minimum value is 7.32 g·cm^{-3} for $x = 0.2$ (~95%). All the samples are highly texturing during SPS-process. The texturing is specific feature of Bi_2Te_3-based alloys, which are sintered from a starting powder, consisting of 2D-particles under uniaxial loading [40–47]. A texturing axis is oriented along mechanical loading direction. Under the texturing, a lamellar grain texture, which is originated from preferential orienting the grains, is forming. The grains are elongated along the lamellar sheets, and the sheets themselves lie in a plane perpendicular to the texturing axis. Resulted from this grains arrangement, crystal *c*-axes of the grains in the lamellar sheets are preferentially directed parallel to the texturing axis, while crystal (*a*-*b*)-planes of the same grains are preferentially oriented perpendicularly to this direction. Forming the texture in the samples is clearly confirmed by SEM and XRD examinations of surfaces, oriented perpendicularly and parallel to the texturing axis (or to SPS-pressing direction). For instance, these SEM images and XRD patterns taken for perpendicular and parallel surfaces of the sample with $x = 0.1$ are shown in Fig. 3. A disordered grain structure with the grains having mainly irregular shape is observed for the perpendicular surface, whereas an ordered grained structure, corresponding to the lamellar sheets, is clearly observed for the parallel surface. Similarly to SEM images, XRD patterns taken on the perpendicular and parallel surfaces are also different. Both XRD patterns are still matching to the $R\bar{3}m$ symmetry, i.e. positions of diffraction peaks are in total agreement with crystal Bi_2Te_3 symmetry, and only redistribution in intensity of the peaks occurs. For the perpendicular surface, the (11 l) peaks are dominant, whereas all other peaks are strongly weakened (Fig. 3(c)). For the surface parallel, the (001) peaks are already dominant (Fig. 3(d)). This intensity redistribution will really take place, if crystal *a*–*b* planes in the grains of textured samples are preferentially oriented perpendicularly to the SPS-pressuring direction.

Average grain sizes corresponding to directions, which are perpendicular ($d_\perp$) and parallel ($d_\parallel$) to the SPS-pressing direction, are remarkably different. To estimate $d_\perp$ and $d_\parallel$, relevant histograms of grain size distribution were plotted which were next analyzed in frames of lognormal unimodal distribution [48]. The $d_\perp$ and $d_\parallel$ equal to ~800 nm and ~80 nm, respectively, are *x*-independent. That is, similarly to the 2D-particles in the starting $Bi_{2-x}Gd_xTe_3$ powders, the grains in the relevant bulk samples are also 2D-objects. The texturing degree of all the samples was characterized by the Lotgering factor, *LF*, which was extracted via analysis of XRD patterns [49]. *LF* can be expressed as

$$F = \frac{p - p_0}{1 - p_0}, \tag{5}$$

where *p* and p_0 are in turn expressed as

$$p = \frac{I(00l)}{\sum I(hkl)} \text{and} p_0 = \frac{I_0(00l)}{\sum I_0(hkl)}. \tag{6}$$

Here, the *I* and I_0 intensities correspond to textured (oriented) and non-textured (non-oriented) samples, respectively. Ideally, $F = 1$ corresponds to completely oriented sample (single crystal), whereas $F = 0$ is characteristic of completely non-oriented sample (powder or grained material with completely random grain orientation).

The *LF*(*x*) dependence is shown in Fig. 4. Depending on deviation in Te-stoichiometry of the bulk $Bi_{2-x}Gd_xTe_{3\pm y}$ samples, which is in turn due to changing the Gd content, this dependence can be divided into two parts. For the first part, which corresponds to the Te-deficient compositions at $x < 0.06$, *LF* is abruptly increasing with increasing *x*. For the second part, which corresponds to the Te-rich compositions at $x > 0.06$, *LF* is increasing much more slowly. This tendency can be related to excess Te content. During SPS-process, some fraction of excess Te can be released as Te inclusions at grain boundaries. It is known [50] that the initial stage of SPS-process is a packing of the particles in the starting powder under external pressuring. During the texturing, the packing results in the rearrangement of the randomly oriented particles into the lamellar sheets with preferential particles orientation. Some nanometer powder lubricants can really improve the particles packing behavior during SPS-process that are earlier reported for the Ce lubricant in Al_2O_3 [51] or the Te lubricant in Bi_2Te_3 [52]. Via the lubricating mechanism, increasing the Te content should result in more effective packing the particles, and relevant increasing in preferential grain orientation. As result, the Lotgering factor will be gradually growing.

Let us consider *x*-effect (or *y*-effect) on the concentration and the Hall mobility of the majority charge carriers in the non-stoichiometric $Bi_{2-x}Gd_xTe_{3\pm y}$ compounds, which were extracted via examination of the Hall effect at room temperature. Since the Hall constant has a negative sign for all the samples being studied, the majority charge carriers in these samples are electrons. The *n*(*x*) and $\mu_H(x)$ dependences are presented in Fig. 5. These dependences are remarkably different for the Te-deficient and Te-rich compositions. With increasing *x*, *n* is steady falling for the Te-deficient compositions, but it is steady rising for the Te-rich compositions. As result,

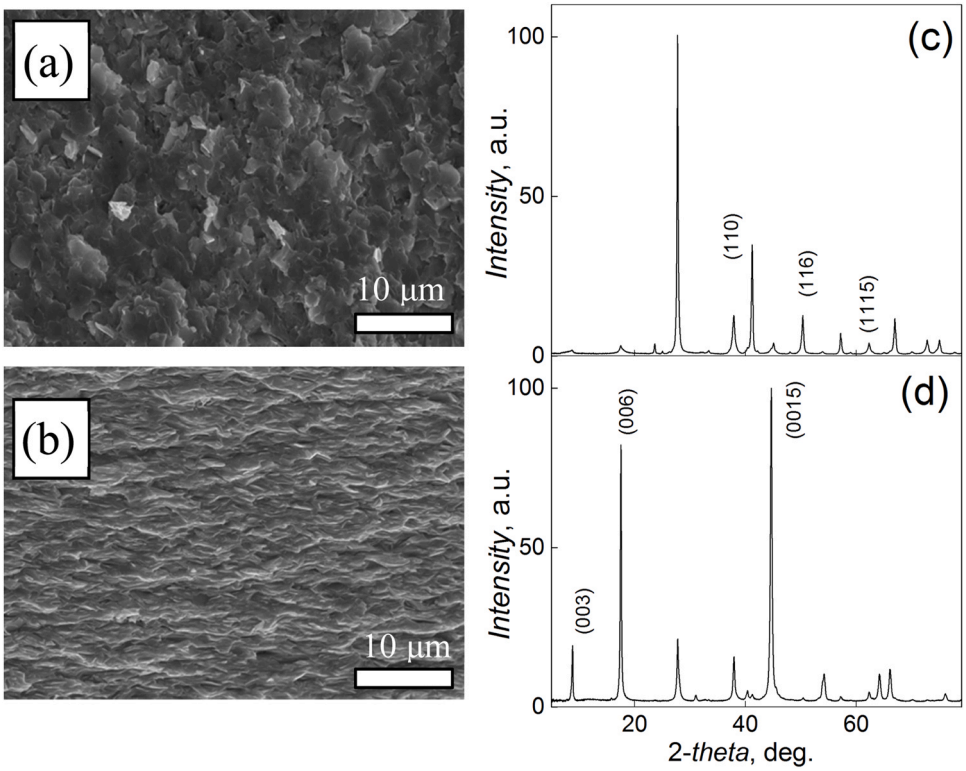

Fig. 3. SEM images taken on the fractured surfaces of the sample with $x = 0.1$, which are oriented perpendicularly (a) and parallel (b) to SPS pressing direction, and XRD patterns taken on perpendicular (c) and parallel (d) surfaces for the same sample.

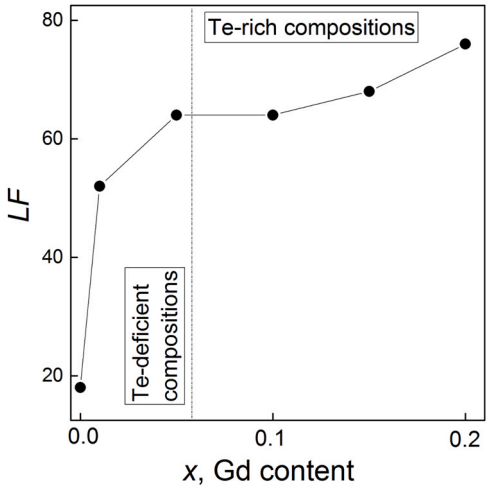

Fig. 4. The Gd content effect on the Lotgering Factor of the bulk $Bi_{2-x}Gd_xTe_{3\pm y}$ samples, SPS-prepared under the same conditions.

minimum n is observed for the composition with $x = 0.05$ and $y = 0.003$. This composition is very close to Te-stoichiometric one. For this composition μ_H is maximal that can be related to less content of various point defects. Generally, both type and concentration of the carriers in Bi_2Te_3 are closely related to various point defects [14–16]. Under the Gd doping, isovalent substitution of Gd^{3+} for Bi^{3+} takes place in the crystal Bi_2Te_3 structure. This substitution cannot directly affect the carriers concentration, but can directly affect the carriers mobility, since the Gd atoms will act as scattering centres for the carriers. However, it is known [17,53–56] that rare earth elements, R, (R=Lu, Tm, Gd, La, Ce, etc.) in fact act as donor centres in the crystal Bi_2Te_3 structure. For the nonstoichiometric Te-deficient $Bi_{2-x}Gd_xTe_{3-y}$ compositions, the vacancies at Te sites, $V_{Te}^{\cdot\cdot}$, and the anti-site Bi_{Te}

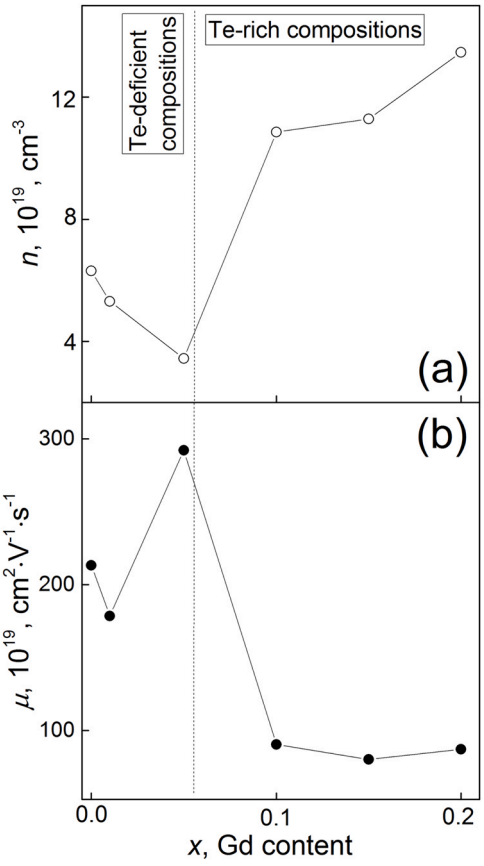

Fig. 5. The Gd content effect on the electron concentration (a) and electron mobility (b) of the bulk $Bi_{2-x}Gd_xTe_{3\pm y}$ samples, SPS-prepared under the same conditions.

defects are the most common defects. These defects are forming via the high-temperature Te evaporation. Forming each positively charged $V_{Te}^{\cdot\cdot}$ vacancy leaves two free electrons as follows

$$Bi_2Te_3 = 2Bi_{Bi}^{\times} + 2Te_{Te}^{\times} + Te(g) + V_{Te}^{\cdot\cdot} + 2e', \quad (7)$$

where symbol g corresponds to a gaseous phase.

A ratio of $V_{Bi}^{\prime\prime\prime}$ and $V_{Te}^{\cdot\cdot}$ vacancies are always equal to 2:3 resulting in a zero net free charge, as shown in Eq. (8).

$$5Bi_2Te_3 = 8Bi_{Bi}^{\times} + 10Te_{Te}^{\times} + 5Te(g) + (2V_{Bi}^{\prime\prime\prime} + 3V_{Te}^{\cdot\cdot}) + 2Bi_{Te} + 2h^{\cdot}. \quad (8)$$

As was mentioned in Introduction part, owing to a small difference in electronegativity between Te and Bi, the anti-site Bi_{Te} defects can be additionally induced, since Bi can easily jump from Bi site to Te site that contributes one hole as a free carrier and, hence, reduces a fraction of the electrons as majority charge carriers. Forming the anti-site Bi_{Te} defects can be also responsible for donor-like effect, which is characteristic for *R*-doped Bi_2Te_3-based compounds [17,53–56]. In this case, the *R*-doping effect on *n* is usually attributed to the difference in electronegativity of atoms forming the anti-site Bi_{Te} and R_{Te} defects that are responsible for holes generation in the crystal Bi_2Te_3 structure. The electronegativity values are equal to 2.10, 2.02 and 1.20 for Te, Bi and Gd, respectively. So, the larger difference in electronegative for Gd-Te pair compared to Bi-Te pair will decrease the concentration of the anti-site defects at Te-sites which contributes one hole per defect and, hence, will result in more electrons. Since the nonstoichiometric Te-rich $Bi_{2-x}Gd_xTe_{3+y}$ compounds are the nonstoichiometric compounds of cation interstitialcy type, the interstitial Te atoms will be intrinsic and typical defects for these compounds [57]. Forming the interstitial Te atoms can be responsible for gradual increasing the lattice *c* parameter with increasing the Te content (Fig. 2(c)). Besides, the anti-site Te_{Bi} defects can be also formed in the Te-rich compositions acting as other point defects. Owing to difference in valence of the Te^{3+} and Bi^{2+} atoms, these point defects will behave as donor centers. As result, the electron concentration in the $Bi_{2-x}Gd_xTe_{3+y}$ compounds will be gradually increasing with increasing excess Te content. This tendency was earlier reported and discussed in Ref. [52]. Finally, releasing the Te inclusions at grain boundaries resulting in increasing the Lotgering factor can take place, too (Fig. 4). This elemental Te could contribute to further increasing *n* through spillover of electrons from these Te inclusions to the $Bi_{2-x}Gd_xTe_{3+y}$ material, owing to the lower work function of the former [52]. Therefore, the $n(x)$ and $\mu_H(x)$ behaviors are dependent on the point defects, which are specific for the Te-deficient and Te-rich compositions. Forming the different point defects degrades of the electron mobility. This degradation will be dependent on defects concentration and ability of the defects to scatter the electrons.

The $n(x)$ and $\mu_H(x)$ behaviors remarkably affect the thermoelectric properties of the non-stoichiometric $Bi_{2-x}Gd_xTe_{3\pm y}$ compounds. Detailed analysis of features in the thermoelectric properties of the nonstoichiometric Te-deficient and Te-rich thermoelectric $Bi_{2-x}Gd_xTe_{3\pm y}$ compounds will be published elsewhere. Here we will just list main features in brief. It is known that the thermoelectric properties of the textured Bi_2Te_3-based compounds, measured parallel or perpendicularly to the texturing axis, are different [40–47]. Better properties allowing maximizing the thermoelectric figure-of-merit are observed for the perpendicular measuring direction. Therefore, only these properties of nonstoichiometric Te-deficient and Te-rich thermoelectric $Bi_{2-x}Gd_xTe_{3\pm y}$ compounds will be examined further. The *x*-dependences of the specific electrical resistivity, ρ_0, the Seebeck coefficient, S_0, and the total thermal conductivity, k_0, measured at room temperature, are presented in Fig. 6 (a), (b) and (c), respectively. Since $\rho = 1/(ne\mu)$, the $\rho_0(x)$ behavior is totally governed by the $n(x)$ and $\mu(x)$ contributions.

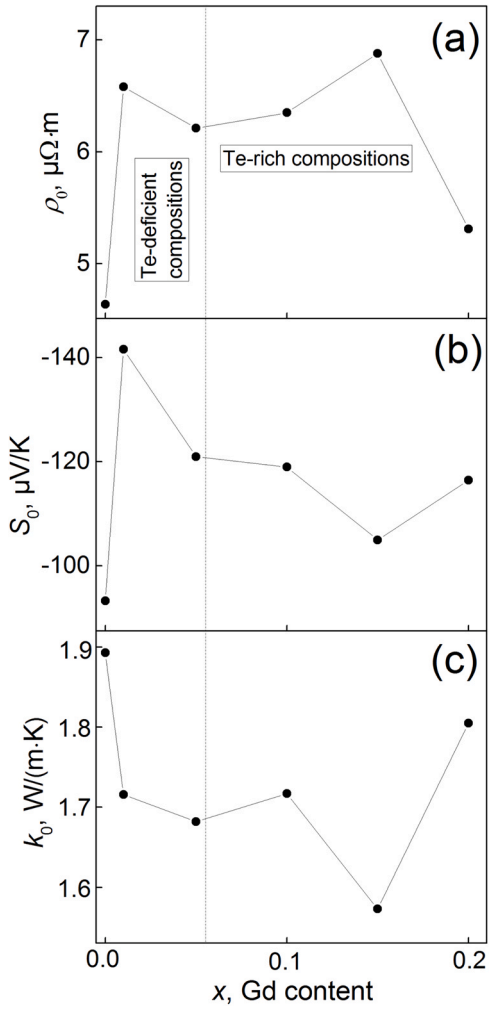

Fig. 6. The Gd content effect on the room temperature thermoelectric properties, ρ_0 (a), S_0 (b) and k_0 (c), of bulk $Bi_{2-x}Gd_xTe_{3\pm y}$ samples, SPS-prepared under the same conditions.

For all the Gd-doped samples, the S_0 values are higher as compared to that for undoped Bi_2Te_3. The highest S_0 value is observed for the Te-deficient composition with $x = 0.01$. The Seebeck coefficient of the degenerate semiconductors can be expressed as

$$S = \frac{2k_B^2 Tm^*}{3e\hbar^2}\left(\frac{\pi}{3n}\right)^{2/3}\left(\frac{3}{2} + \gamma\right), \quad (9)$$

where k_B is the Boltzmann's constant, $\hbar$ is the reduced Planck constant, m^* is the density-of-state effective mass of electrons and γ is the scattering factor.

Expression (9) shows that the higher concentration of electrons decreases *S*. Normally, increasing ρ will be accompanied by increasing *S*. This tendency is observed for the Te-deficient compositions, whereas the ρ-*S* link for the Te-rich compositions is opposite. Possible changing γ, which can be related to forming different point defects in the Te-deficient and Te-rich compositions, should be taken into account to explain this feature.

The k_0 values for all the Gd-doped compositions are lower as compared to that for undoped Bi_2Te_3. This feature can be attributed to, firstly, changing the electron contribution into the total thermal conductivity, and, secondly, changing the phonon contribution into the thermal conductivity, which is related to forming the specific point defects scattering phonons.

The temperature dependences of ρ, *S* and power factor $PF=S^2/\rho$, taken for $Bi_{2-x}Gd_xTe_{3\pm y}$ samples with different *x*, are shown in

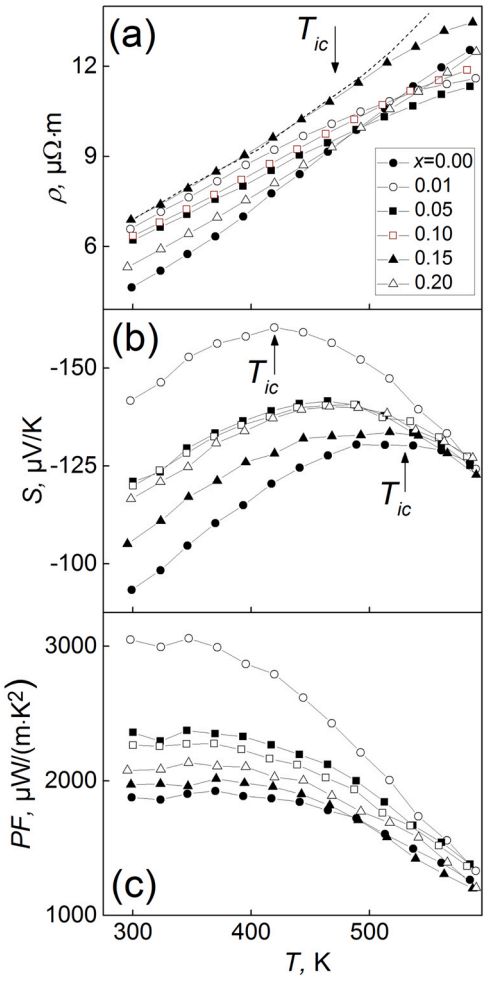

Fig. 7. The Gd content effect on temperature behavior of ρ (a), S (b) and PF (c) of bulk $Bi_{2-x}Gd_xTe_{3\pm y}$ samples, SPS-prepared under the same conditions.

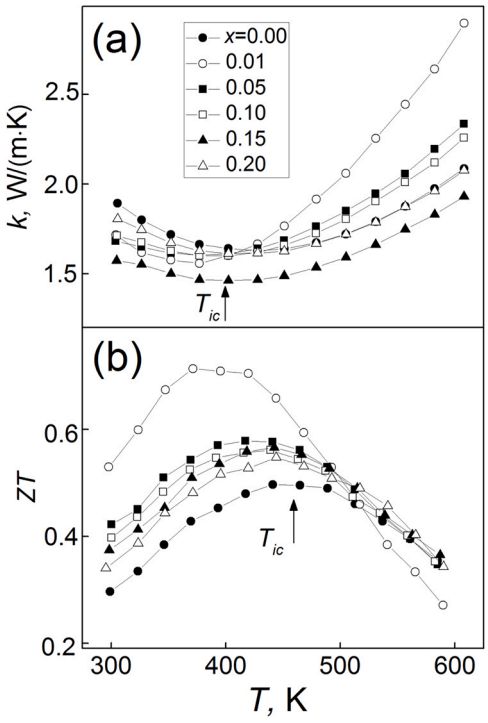

Fig. 8. The Gd content effect on temperature behavior of k (a) and ZT (b) of bulk $Bi_{2-x}Gd_xTe_{3\pm y}$ samples, SPS-prepared under the same conditions.

Fig. 7(a), (b) and (c), respectively. The temperature dependences of k and ZT of these samples are presented in Fig. 8(a) and (b). Main features in the $\rho(T)$, $S(T)$, $k(T)$ and $ZT(T)$ behavior are typical for the Bi_2Te_3 and Bi_2Te_3-based compounds [17,53–56]. These features are mainly due to onset of intrinsic conductivity at high temperatures that is originated from a thermal excitation of carriers from valence band to conduction band. The intrinsic conductivity onset, indicated by arrows at temperature T_{ic} in Figs. 7 and 8, results in appearance of kinks in the $\rho(T)$ dependences (Fig. 7(a)), minima in the $k(T)$ dependences (Fig. 8(a)), and maxima in the $S(T)$ and $ZT(T)$ dependences (Figs. 7(b) and 8(b)). To not complicate Fig. 7(a) and (b), the arrows are shown only for some x values. Detailed explanations of physical mechanisms, resulting in changing the thermoelectric properties at T_{ic}, can be found in Refs. [17,53–56]. The highest ZT value equal to ~0.7 at ~400 K is observed for Te-deficient $Bi_{2-x}Gd_xTe_{3-y}$ composition with $x = 0.01$ and $y = 0.011$. Although ρ for this composition is higher than ρ for the compositions with $x = 0$; 0.05; 0.1 and 0.2, especially below T_{ic}, but its S value is highest among all the compositions. As result, PF of this composition is also maximal within entire temperature range under consideration. The thermal conductivity of the composition with $x = 0.01$ measured below T_{ic} is low enough, too. Owing to the low k and high PF values, this nonstoichiometric Te-deficient composition demonstrates the highest thermoelectric figure-of-merit ($ZT \approx 0.7$ at ~400 K).

It should be also noted that Gd is transient f-metal with ferromagnetic ordering, which takes place below 292 K [57]. Magnetic moments of the Gd atoms, embedded in solid, can remarkably affect its properties. For instance, the Kondo effect and various types of magnetic ordering can be often observed in solid with magnetic impurities. Bi_2Te_3 is known to be topological insulator [58]. Currently, embedding magnetic impurities in topological insulator is fruitful way to explore features in the topological properties. However, various physical phenomena, which are characteristic of solid with magnetic impurities, are usually observed at low temperatures (below ~50 K). In this paper, the properties of Te-deficient and Te-rich thermoelectric $Bi_{2-x}Gd_xTe_{3\pm y}$ compounds were studied above room temperature. Hence, we did not take into account magnetic effects of the Gd dopants on properties of these compounds. However, research of low-temperature transport properties of the compounds in progress.

4. Conclusion

Thus, the solvothermal synthesis and spark plasma sintering methods have been applied to prepare the Gd-doped Bi_2Te_3 compounds. For the $Bi_{2-x}Gd_xTe_{3\pm y}$ compounds with $x = 0.01$; 0.05; 0.1; 0.15 and 0.2, the Gd doping resulted in relevant changing the Te content, y, i.e. x and y happened to be inter-dependent. Depending on the Gd content, the Te-deficient $Bi_{2-x}Gd_xTe_{3-y}$ compositions with $x = 0$; 0.01; 0.05 and $y = 0.018$; 0.011; 0.003, and the Te-rich $Bi_{2-x}Gd_xTe_{3+y}$ compositions with $x = 0.1$; 0.15; 0.2 and $y = 0.013$; 0.023; 0.04 could be prepared. Destroying Te-stoichiometry is due to high-temperature Te evaporation under SPS-process. To tune desired deviation from Te-stoichiometry, the Te-enriched starting $Bi_{2-x}Gd_xTe_3$ powders were used. With increasing x, a rate of this Te evaporation remarkably decreases that is related to more strength of the chemical Gd-Te bond as compared to that for the Bi-Te bond. Difference in electronegativites of the Bi and Gd atoms, which results in increasing the ionic bonding degree, can result in strengthen of this bond. The lattice parameters, electron concentration and electron mobility, and, hence, thermoelectric properties, as well as the grain ordering degree are quite different for the nonstoichiometric Te-deficient and Te-rich compositions. This difference can be attributed

to specific defects forming in these compositions. The Te-vacancies and the anti-site Bi_{Te} defects are specific for the Te-deficient compositions, whereas the interstitial Te atoms and the anti-site Te_{Bi} defects are characteristic for the Te-rich compositions.

CRediT authorship contribution statement

Oleg Ivanov: Writing – review & editing. **Maxim Yaprintsev**: Investigation. **Alexei Vasil'ev**: Investigation.

Declaration of Competing Interest

The authors declare that they have no known competing financial interests or personal relationships that could have appeared to influence the work reported in this paper.

Acknowledgements

This work was supported by the Ministry of Science and Higher Education of Russian Federation (grant number No 0625-2020-0015). All of studies were carried out by the scientific equipment of joint research centre "Technologies and Materials" at the Belgorod State University.

References

[1] G.J. Snyder, Figure of merit ZT of a thermoelectric device defined from materials properties, Energy Environ. Sci. 10 (2017) 2280–2283, https://doi.org/10.1039/c7ee02007d
[2] W. Saito, K. Hayashi, J. Dong, J.F. Lee, Y. Miyazaki, Control of the thermoelectric properties of Mg_2Sn single crystals via point-defect engineering, Sci. Rep. 10 (2020) 1–8, https://doi.org/10.1038/s41598-020-58998-1 (2020).
[3] G. Guelou, C. Couder, A. Bourhim, O. Lebedev, N. Daneu, A scalable synthesis route for multiscale defect engineering in the sustainable thermoelectric quaternary sulfide $Cu_{26}V_2Sn_6S_{32}$, Acta Mater. 195 (2020) 229–239, https://doi.org/10.1016/j.actamat.2020.05.039
[4] Y. Anno, Y. Imakita, K. Takei, S. Akita, T. Arie, Enhancement of graphene thermoelectric performance through defect engineering, 2D Mater. 4 (2017) 1–6, https://doi.org/10.1088/2053-1583/aa57fc (025019).
[5] X. Dong, W. Cui, W.-D. Liu, S. Zheng, L. Gao, L. Yue, Y. Wue, B. Wang, Z. Zhang, L. Chen, Z.-G. Chen, Synergistic band convergence and defect engineering boost thermoelectric performance of SnTe, J. Mater. Sci. Technol. 86 (2021) 204–209, https://doi.org/10.1016/j.jmst.2021.01.040
[6] O. Ivanov, M. Yaprintsev, A. Vasil'ev, E. Yaprintseva, Microstructure and thermoelectric properties of the medium-entropy block-textured $BiSbTe_{1.5}Se_{1.5}$ alloy, J. Alloy. Compd. 872 (2021) 1–7, https://doi.org/10.1016/j.jallcom.2021.159743 (159743).
[7] Y. Zheng, T.J. Slade, L. Hu, X.Y. Tan, Y. Luo, Z.-Z. Luo, J. Xu, Q. Yan, M.G. Kanatzidis, Defect engineering in thermoelectric materials: what have we learned? Chem. Soc. Rev. 50 (2021) 9022–9054, https://doi.org/10.1039/D1CS00347J
[8] C. Zhou, Y.K. Lee, J. Cha, B. Yoo, S.P. Cho, T. Hyeon, I. Chung, Defect engineering for high-performance n-type PbSe thermoelectrics, J. Am. Chem. Soc. 140 (2018) 9282–9290, https://doi.org/10.1021/jacs.8b05741
[9] J. Mao, Y. Wu, S. Song, Q. Zhu, J. Shuai, Z. Liu, Y. Pei, Z. Ren, Defect engineering for realizing high thermoelectric performance in n-type Mg_3Sb_2-based materials, ACS Energy Lett. 2 (2017) 2245–2250, https://doi.org/10.1021/acsenergylett.7b00742
[10] Z. Du, J. He, X. Chen, M. Yan, J. Zhu, Y. Liu, Point defect engineering in thermoelectric study of InSb, Intermetallics 112 (2019) 1–10, https://doi.org/10.1016/j.intermet.2019.106528 (106528).
[11] H.J. Goldsmid, Bismuth telluride and its alloys as materials for thermoelectric generation, Materials 7 (2014) 2577–2592, https://doi.org/10.3390/ma7042577
[12] H. Scherrer, S. Scherrer, Thermoelectrics Handbook: Macro to Nano, CRC Taylor and Francis, Boca Raton, 2012.
[13] G.S. Nolas, J. Sharp, H.J. Goldsmid, Thermoelectrics Basic Principles and New Materials Developments, Springer, Berlin, 2001.
[14] Y. Pan, T.R. Wei, C.F. Wu, J.F. Li, Electrical and thermal transport properties of spark plasma sintered n-type $Bi_2Te_{3-x}Se_x$ alloys: the combined effect of point defect and Se content, J. Mater. Chem. C 3 (2015) 10583–10589, https://doi.org/10.1039/C5TC02219C
[15] L. Hu, T. Zhu, X. Liu, X. Zhao, Point defect engineering of high-performance bismuth-telluride-based thermoelectric materials, Adv. Funct. Mater. 24 (2014) 5211–5218, https://doi.org/10.1002/adfm.201400474
[16] J. Suh, K.M. Yu, D. Fu, X. Liu, F. Yang, J. Fan, D.J. Smith, Y.H. Zhang, J.K. Furdyna, C. Dames, W. Walukiewicz, J. Wu, Simultaneous enhancement of electrical conductivity and thermopower of Bi_2Te_3 by multifunctionality of native defects, Adv. Mater. 27 (2015) 3681–3686, https://doi.org/10.1002/adma.201501350
[17] O. Ivanov, M. Yaprintsev, R. Lyubushkin, O. Soklakova, Enhancement of thermoelectric efficiency in Bi_2Te_3 via rare earth element doping, Scr. Mater. 146 (2018) 91–94, https://doi.org/10.1016/j.scriptamat.2017.11.031
[18] M. Yaprintsev, A. Vasil'ev, O. Ivanov, M. Zhezhu, E. Yaprintseva, V. Novikov, Enhanced thermoelectric efficiency of the bulk composites consisting of "Bi_2Te_3 matrix" and "filler $Ni@NiTe_2$ inclusions", Scr. Mater. 194 (2021), https://doi.org/10.1016/j.scriptamat.2020.113710 (113710-1-4).
[19] Y. Liu, M. Zhou, J. He, Towards higher thermoelectric performance of Bi_2Te_3 via defect engineering, Scr. Mater. 111 (2015) 39–73, https://doi.org/10.1016/j.scriptamat.2015.06.031
[20] Y. Pan, U. Aydemir, J.A. Grovogui, I.T. Witting, R. Hanus, Y. Xu, J. Wu, C.-F. Wu, F.-H. Sun, H.-L. Zhuang, J.-F. Dong, J.-F. Li, V.P. Dravid, G.J. Snyder, Melt-centrifuged $(Bi,Sb)_2Te$: engineering microstructure toward high thermoelectric efficiency, Adv. Mater. 30 (2018) 1–7, https://doi.org/10.1002/adma.201802016 (1802016).
[21] H. Zhu, J.-Y. Zhao, C. Xiao, Improved thermoelectric performance in n-type BiTe facilitated by defect engineering, Rare Met. 40 (2021) 2829–2837, https://doi.org/10.1007/s12598-021-01737-w
[22] M. Hong, Z.-G. Chen, J. Zou, Fundamental and progress of Bi_2Te_3-based thermoelectric materials, Chin. Phys. B 27 (2018) 1–46, https://doi.org/10.1088/1674-1056/27/4/048403 (048403).
[23] L. Hu, T. Zhu, X. Liu, X. Zhao, Point defect engineering of high-performance bismuth-telluride-based thermoelectric materials, Adv. Funct. Mater. 24 (2014) 5211–5218, https://doi.org/10.1002/adfm.201400474
[24] F. Elmakaty, K.A. Mkhoyan, K.M. Youssef, The effects of structural integrity of graphene on the thermoelectric properties of the n-type bismuth-telluride alloy, J. Alloy. Compd. 876 (2021) 1–9, https://doi.org/10.1016/j.jallcom.2021.160198 (160198).
[25] F. Wu, H. Song, J. Jia, X. Hu, Effects of Ce, Y, and Sm doping on the thermoelectric properties of Bi_2Te_3 alloy, Prog. Nat. Sci. Mater. Int. 23 (2013) 408–412, https://doi.org/10.1016/j.pnsc.2013.06.007
[26] J. Lee, A. Berger, L.U. Cagnon, U. Gosele, K. Nielsch, J. Lee, Disproportionation of thermoelectric bismuth telluride nanowires as a result of the annealing process, Phys. Chem. Chem. Phys. 12 (2010) 15247–15250, https://doi.org/10.1039/c0cp00749h
[27] P. Lost'ák, C. Drasar, D. Bachan, L. Benes, A. Krejcová, Defects in $Bi_2Te_{3-x}Se_x$ single crystals, Radiat. Eff. Defects Solids 165 (2010) 211–215, https://doi.org/10.1080/10420151003616663
[28] T. Zhu, L. Hu, X. Zhao, J. He, New insights into intrinsic point defects in V_2VI_3 thermoelectric materials, Adv. Sci. 3 (2016) 1–16, https://doi.org/10.1002/advs.201600004 (1600004).
[29] S.-W. Kim, M.-H. Jung, Gd doping effect in p-type Bi_2Te_3 single crystals, AIP Adv. 8 (2018) 101319, https://doi.org/10.1063/1.5042494-1-6
[30] Y.Q. Jia, Crystal radii and effective ionic radii of the rare earth ions, J. Sol. State Chem. 95 (1991) 184–187, https://doi.org/10.1016/0022-4596(91)90388-X
[31] J.R. Drabble, C.H.L. Goodman, Chemical bonding in bismuth telluride, J. Phys. Chem. Solids 5 (1958) 142–144, https://doi.org/10.1016/0022-3697(58)90139-2
[32] S. Nakajima, The crystal structure of $Bi_2Te_{3-x}Se_x$, J. Phys. Chem. Solids 24 (1963) 479–485, https://doi.org/10.1016/0022-3697(63)90207-5
[33] M. Yaprintsev, A. Vasiliev, O. Ivanov, Sintering temperature effect on thermoelectric properties and microstructure of the grained $Bi_{1.9}Gd_{0.1}Te_3$ compound, J. Eur. Ceram. Soc. 39 (2019) 1193–1205, https://doi.org/10.1016/j.jeurceramsoc.2018.12.041
[34] R.T. Sanderson, Electronegativity and bond energy, J. Am. Chem. Soc. 105 (1983) 2259–2261, https://doi.org/10.1021/ja00346a026
[35] G.D. Sproul, Evaluation of electronegativity scales, ACS Omega 5 (2020) 11585–11594, https://doi.org/10.1021/acsomega.0c00831
[36] P. Manka, A relation between the binding energy and the band-gap energy in semiconductors of diamond or zinc-blende structure, J. Phys. Chem. Sol. 20 (1961) 268–273, https://doi.org/10.1016/0022-3697(61)90013-0
[37] A.K. Vijh, Correlation between bond energies and forbidden gaps of inorganic binary compounds, J. Phys. Chem. Sol. 30 (1969) 1999–2005, https://doi.org/10.1016/0022-3697(69)90178-4
[38] L. Pauling, The Nature of the chemical bond', Oxford & IBH Pub. Co., Delhi, (1969).
[39] H. Fang, J.-H. Bahk, T. Feng, Z. Cheng, A.M. Mohammed, X. Wang, X. Ruan, A. Shakouri, Y. Wu, Thermoelectric properties of solution synthesized n-type Bi_2Te_3 nanocomposites modulated by Se: an experimental and theoretical study, Nano Res. 9 (2016) 117–127, https://doi.org/10.1007/s12274-015-0892-x
[40] M. Yaprintsev, A. Vasil'ev, O. Ivanov, Thermoelectric properties of the textured $Bi_{1.9}Gd_{0.1}Te_3$ compounds spark-plasma-sintered at various temperatures, J. Eur. Ceram. Soc. 40 (2020) 742–750, https://doi.org/10.1016/j.jeurceramsoc.2018.12.041
[41] S.D. Bhame, D. Pravarthana, W. Prellier, J.G. Noudem, Enhanced thermoelectric performance in spark plasma textured bulk n-type $Bi_2Te_{2.7}Se_{0.3}$ and p-type $Bi_{0.5}Sb_{1.5}Te_3$, Appl. Phys. Lett. 102 (2013) 1–3, https://doi.org/10.1063/1.4807771 (2190).
[42] X.A. Fan, J.Y. Yang, R.G. Chen, H.S. Yun, W. Zhu, S.Q. Bao, X.K. Duan, Characterization and thermoelectric properties of p-type 25%Bi_2Te_3–75%Sb_2Te_3 prepared via mechanical alloying and plasma activated sintering, J. Phys. D Appl. Phys. 39 (2006) 740–745, https://doi.org/10.1088/0022-3727/39/4/021
[43] J. Jiang, L. Chen, S. Bai, Q. Yao, Q. Wang, Fabrication and thermoelectric performance of textured n-type $Bi_2(Te,Se)_3$ by spark plasma sintering, Mater. Sci. Eng. B 117 (2005) 334–338, https://doi.org/10.1016/j.mseb.2005.01.002
[44] Q. Lognon, F. Gascoin, O.I. Lebedev, L. Lutterotti, S. Gascoin, D. Chateigner, Quantitative texture analysis of spark plasma textured n-Bi_2Te_3, J. Am. Ceram. Soc. 97 (2014) 2038–2045, https://doi.org/10.1111/jace.12970/

[45] A. Vasil'ev, M. Yaprintsev, O. Ivanov, E. Danshina, Anisotropic thermoelectric properties of $Bi_{1.9}Lu_{0.1}Te_{2.7}Se_{0.3}$ textured via spark plasma sintering, Solid State Sci. 84 (2018) 28–430, https://doi.org/10.1016/j.solidstatesciences.2018.08.004
[46] S. Miura, Y. Satob, K. Fukuda, K. Nishimura, K. Ikeda, Texture and thermoelectric properties of hot-extruded Bi_2Te_3 compound, Mater. Sci. Eng. A 277 (2000) 244–249, https://doi.org/10.1016/S0921-5093(99)00539-0
[47] O. Ivanov, M. Yaprintsev, A. Vasil'ev, Comparative analysis of the thermoelectric properties of the non-textured and textured $Bi_{1.9}Gd_{0.1}Te_3$ compounds, J. Solid State Chem. 290 (2020), https://doi.org/10.1016/j.jssc.2020.121559
[48] F.J. Humphreys, M. Hatherly, Recrystallization and Related Annealing Phenomena, Elsevier, Oxford, UK, 2004.
[49] F.K. Lotgering, Topotactical reactions with ferrimagnetic oxides having hexagonal crystal structures—I, J. Inorg. Nucl. Chem. 9 (1959) 113–123, https://doi.org/10.1016/0022-1902(59)80070-1
[50] L. Wang, V. Pouchly, K. Maca, Z. Shen, Y. Xiong, Intensive particle rearrangement in the early stage of spark plasma sintering process, J. Asian Ceram. Soc. 3 (2015) 183–187, https://doi.org/10.1016/j.jascer.2015.02.004
[51] I. Alvarez-Clemares, G. Mata-Osoro, A. Fernandez, S. Lopez-Esteban, C. Pecharroman, J. Palomares, R. Torrecillas, J.Serafın Moya, Transparent alumina/ceria nanocomposites by spark plasma sintering, Adv. Eng. Mater. 12 (2010) 1154–1160, https://doi.org/10.1002/adem.201000176
[52] Y. Liu, Y. Zhang, K.H. Lim, M. Ibáñez, S. Ortega, M. Li, J. David, S. Martí-Sánchez, K.M. Ng, J. Arbiol, M.V. Kovalenko, D. Cadavid, A. Cabot, High thermoelectric performance in crystallographically textured n-type $Bi_2Te_{3-x}Se_x$ produced from asymmetric colloidal nanocrystals, ACS Nano 12 (2018) 7174–7184, https://doi.org/10.1021/acsnano.8b03099
[53] M. Yaprintsev, R. Lyubushkin, O. Soklakova, O. Ivanov, Effects of Lu and Tm doping on thermoelectric properties of Bi_2Te_3, J. Electron. Mater. 47 (2018) 1362–1370, https://doi.org/10.1007/s11664-017-5940-8
[54] O. Ivanov, M. Yaprintsev, Mechanisms of thermoelectric efficiency enhancement in Lu-doped Bi_2Te_3, Mater. Res. Express 5 (2018), https://doi.org/10.1088/2053-1591/aaa265
[55] J. Yang, F. Wu, Z. Zhu, L. Yao, H. Song, X. Hu, Thermoelectrical properties of lutetium-doped Bi_2Te_3 bulk samples prepared from flower-like nanopowders, J. Alloy. Compd. 619 (2015) 401–405, https://doi.org/10.1016/j.jallcom.2014.09.024
[56] X.H. Ji, X.B. Zhao, Y.H. Zhang, B.H. Lu, H. Ni, Synthesis and properties of rare earth containing Bi2Te3 based thermoelectric alloys, J. Alloy. Compd. 387 (2005) 282–286, https://doi.org/10.1016/j.jallcom.2004.06.047
[57] B.D. Cullity, C.D. Graham, Introduction to Magnetic Materials, IEEE Press, Piscataway, 2009.
[58] H. Osterhage, J. Gooth, B. Hamdou, P. Gwozdz, R. Zierold, K. Nielsch, Thermoelectric properties of topological insulator Bi_2Te_3, Sb_2Te_3, and Bi_2Se_3 thin film quantum wells, Appl. Phys. Lett. 105 (2014), https://doi.org/10.1063/1.4896680 (123117 -1-4).